

# INTERNSHIP REPORT

M2 Frontiers in Chemistry Master's program  
2024-2025

## Advanced analysis of pitting corrosion using optical and electrochemical techniques enhanced by AI

Anes SADAoui

Supervised by Dr. Viacheslav SHKIRSKIY



February 3rd 2025 - August 1st 2025

# Contents

<b>List of figures</b>	<b>2</b>
<b>List of tables</b>	<b>3</b>
<b>Abstract</b>	<b>4</b>
<b>Introduction</b>	<b>6</b>
1    Results and discussion . . . . .	7
1.1    Statistical analysis : particle angle of ejection . . . . .	7
1.1.1    Preferential angles of ejection . . . . .	8
1.1.2    Corelation between pit's propagation and angle of ejection of particles . . . . .	9
1.1.3    Image treatment and general flux behavior . . . . .	10
1.1.4    Particle trajectory outliers . . . . .	11
1.1.5    Limitations of classical computer vision tools . . . . .	12
1.2    Deep learning approach : enhanced particle segmentation and detection using CNNs . . . . .	13
1.2.1    U-Net architecture and training . . . . .	13
1.2.2    Model performance . . . . .	15
<b>Conclusion</b>	<b>17</b>
<b>Bibliography</b>	<b>18</b>
<b>Appendix</b>	<b>19</b>

## List of Figures

1	(a) Chemical composition of each layer of stainless steel 316L ; (b) General scheme of chemical reactions happening at the interface solution/metal in pits <sup>1</sup> .	7
2	Full frame and zoom onto a pit region. Green circles highlight corrosion products	
	(a). pre-processing of images (b). . . . .	7
3	<i>Particle (highlighted in green) angle calculation with reference point in the center of the pit.</i> . . . . .	8
4	Polar plot of overall angles of ejections around considered pits . . . . .	8
5	<i>Raw images of a single pit propagation at frame 30, 50, 100, 200 (top) and subtracted images at the same frame (frame 30 is subtracted with frame 0, frame 50 is subtracted with frame 30 ...) (bottom).</i> . . . . .	9
6	<i>Cross-correlation between the ejection angle of particles and propagation angle of pit versus the frame lag</i> . . . . .	9
7	<i>Corrosion products movement within the sample for 30 mM and 100 mM of NaCl in solution. Particle traces are shown in green.</i> . . . . .	10
8	<i>Tracking of a single particle taken in the vicinity of a pit in a 30 mM sample. Red circle highlights the particle of interest.</i> . . . . .	11
9	<i>Evolution of the velocity in px/frame of the considered particle in Figure 8 between frame 190 (being frame 0 on the x axis) and frame 300 (being frame 110 on the x axis). Red rectangle corresponds to a velocity outlier</i> . . . . .	12
10	<i>Subtracted image of the considered particle and its surrounding at the frame 291. Corresponding to the moment right before the velocity peak. Red arrow points the direction of the particle movement.</i> . . . . .	12
11	<i>Raw image (Raw), enhanced contrast image with CLAHE (CLAHE), particle segmentation using state of the art contouring / morphological treatment (Classical) and manual segmentation of particles (Manual)</i> . . . . .	13
12	<i>U-Net architecture<sup>2</sup></i> . . . . .	14
13	<i>Slice of a raw image, manually labeled image (GROUND TRUTH) and prediction of the model (PREDICTION) for a 30 mM sample.</i> . . . . .	15
14	<i>From left to right : raw image, predicted mask of particles by U-Net and obtained mask using state of the art image processing and contouring.</i> . . . . .	16

## List of Tables

- 1    *Performance table of U-Net at different values of epochs and learning rate. Performance at different learning rates have been calculated at 100 epochs . . . . .* 16

## **Abstract (English)**

Knowledge about the mechanisms underlined by pitting corrosion has stagnated for several years now, while the amount of data — ranging from microscopy images to electrochemical data — is more important than ever. The future evolution of the insights in this field could reside in a more data-driven science than a traditional one. This report presents a data-driven approach based on the use of deep learning and computer vision to harvest key parameters in microscopic images of pitting corrosion. A preliminary statistical analysis on corrosion products/particles ejecting from pits, shows a clear preferential ejection direction of particles toward certain angles. It also shows a vertical component of the ejection that was never considered before. This preliminary study also shows a statistically significant link between the horizontal pit propagation direction and the ejection direction of the particles. The report also details the development of computer vision and deep learning based tools to enhance the previous analysis and get even more insights on particle ejection. This tool, by using a trained convolutional neural network, shows a great performance on segmenting the particles that will help correctly track them and gain even more insights on their behavior during the ejection. Image processing has also revealed the general behavior of the flux at the origin of the particles movement.

## Abstract (French)

La compréhension des mécanismes à l'origine de la corrosion par piqûres stagne depuis plusieurs années, alors même que la quantité de données disponibles — allant des images de microscopie aux données électrochimiques — n'a jamais été aussi importante. L'évolution future des connaissances dans ce domaine pourrait résider dans une science davantage axée sur les données que dans une approche traditionnelle. Ce rapport présente une méthode fondée sur l'utilisation de l'apprentissage profond et de la vision par ordinateur pour extraire des paramètres clés à partir d'images microscopiques de corrosion par piqûres. Une analyse statistique préliminaire des produits ou particules de corrosion éjectés des piqûres révèle une direction d'éjection préférentielle claire vers certains angles. Elle met également en évidence une composante verticale de l'éjection qui n'avait jamais été prise en compte auparavant. Cette étude préliminaire montre également un lien statistiquement significatif entre la direction de propagation horizontale de la piqûre et la direction d'éjection des particules..

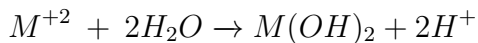
Le rapport détaille également le développement d'outils basés sur la vision par ordinateur et l'apprentissage profond visant à approfondir l'analyse précédente et à obtenir encore plus d'informations sur l'éjection des particules. Cet outil, en s'appuyant sur un réseau de neurones convolutifs entraîné, montre d'excellentes performances pour segmenter les particules, ce qui permettra de mieux les suivre et de mieux comprendre leur comportement lors de l'éjection. Le traitement d'images a également permis de révéler le comportement général du flux à l'origine du mouvement des particules.

## Introduction

Natural corrosion of metals results in global economic losses averaging around 2,500 billion dollars annually, representing between 2.5 % and 4.5 % of global GDP. This phenomenon, occurring since ancient times, presents a significant issue in various industrial sectors, including aeronautics, naval, nuclear, and others, where corrosion poses not only economic concerns but also critical safety threats.

Corrosion itself involves the dissolution of bulk metal material when exposed to specific chemical agents, weakening the structural integrity and potentially leading to collapse. To mitigate this, numerous metal alloys have been engineered to naturally form a protective passive film on their surfaces, thereby reducing corrosion rates. However, this protective film often develops unevenly, resulting in localized areas with heightened corrosion vulnerability<sup>3</sup>, particularly in the presence of chemicals like alkaline compounds. Such localized corrosion is known as pitting corrosion.

Pitting corrosion has been extensively studied, and its stages are well-documented. The fundamental mechanism involves a dynamic balance among passivation, breakdown, and re-passivation of the protective film. Disruption of this balance leads to the formation of corrosion pits, which can either continue to expand through dissolution of bulk metal into the surrounding environment (stable pits) or re-passivate (unstable pits)<sup>4</sup>. Many parameters could influence this dynamic, such as the pH of the solution inside the pit that becomes more acid because of the metal ions hydrolysis following this reaction<sup>5</sup> :



Also, chloride known for attacking chromium passive film is a key factor in the pitting dynamic. The existing scientific literature offers comprehensive insights into the formation, disruption, and subsequent growth of pits but lacks of comprehension on certain phenomenon such as the behavior of corrosion products.

In this report, our focus will be on stainless steel 316L, one of the most commonly used alloys across various industries. Figure 1 illustrates the chemical composition of the different layers within stainless steel 316L and details the typical pitting corrosion mechanism occurring in the presence of chlorides. Once the passive film is disrupted, the bulk iron of the metal is exposed directly to the corrosive solution, acting as an anode and dissolving into iron ions ( $Fe^{3+}$  or  $Fe^{2+}$ ). Subsequently, these ions often react within the solution, forming iron oxides and iron hydroxides, known as corrosion products. Understanding the behavior and aggregation of these corrosion products near corrosion pits is essential, as they significantly influence pit dynamics, potentially facilitating re-passivation and affecting the overall corrosion process or ejects far from the pit through a driving force that we haven't fully grasped yet.

This study focuses on analyzing the behavior of particle ejection, highlighting how computer vision and deep learning techniques using python can improve particle detection and aid in quantifying their dynamics<sup>6</sup>.

The object of our study is a database comprising seven corrosion videos, each one corresponding to a certain concentration of NaCl in the solution (5mM, 10mM, 10mM(2), 30mM, 30mM(2), 50mM, 100mM)<sup>7</sup>. The recording setup is presented in Appendix B. Each video has a resolution of 2240x2252 pixels and was captured at a frame rate of 15 Hz. The spatial resolution corresponds to a pixel size of 480x480 nm.



Figure 1: (a) Chemical composition of each layer of stainless steel 316L ; (b) General scheme of chemical reactions happening at the interface solution/metal in pits<sup>1</sup>

This study provides a preliminary statistical analysis of the ejection behavior of corrosion particles, utilizing classical computer vision techniques implemented notably via the python OpenCV library. The limitations of these traditional approaches will be discussed, and development of advanced tools leveraging deep learning, particularly famous convolutional neural networks (CNNs) U-Net, will be explained. These novel approaches aim to improve the detection and segmentation quality of corrosion particles, enabling more accurate insights into their dynamic behavior.

## 1 Results and discussion

### 1.1 Statistical analysis : particle angle of ejection

Figure 2 (a) shows the full image recorded during the corrosion process, revealing the formation of pits. We can also observe small dark objects being ejected from the pit in what appears, at first glance, to be a stochastic manner. To verify this hypothesis, we applied computer vision techniques based on object contour detection using python to track the particles and quantify their ejection angles, allowing us to assess whether the behavior is truly stochastic or not.

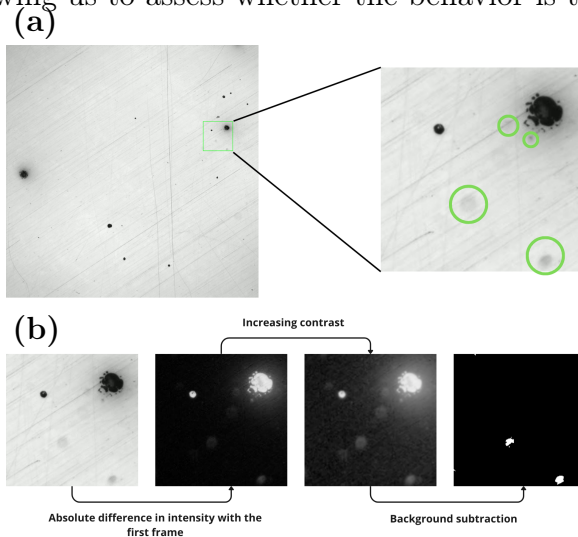


Figure 2: Full frame and zoom onto a pit region. Green circles highlight corrosion products (a). pre-processing of images (b).

Figure 2(b) illustrates the image processing steps used to enhance contrast and facilitate particle detection, along with the resulting segmentation. First, the first frame of the video has been subtracted from the image in order to keep only new pixels, then an histogram equalization was applied to the frame to improve contrast, Finally, background subtractor<sup>8</sup> (MOG2) was used to isolate moving pixels, which correspond to the ejected particles.

### 1.1.1 Preferential angles of ejection

The blurred and coarse appearance of the particles is due to their position being out of the microscope's focal plane. Each particle's position was tracked over time, and its ejection angle was recorded at each time point. This angle is measured in degrees relative to the horizontal axis (blue line), using the center of the stable pit as the reference point, as illustrated in Figure 3. Angles range from 0° to 360° and increase in the clockwise direction. A polar plot is then made from all the angles recorded at each frame of the video.

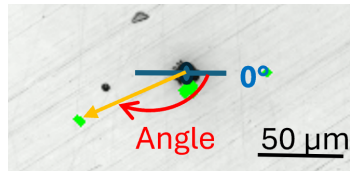


Figure 3: *Particle (highlighted in green) angle calculation with reference point in the center of the pit.*

The polar plots shown in Figure 4 indicate that some pits exhibit a preferential ejection angle, while others eject particles in a more isotropic manner. Pits displaying directional ejection do not show any distinguishing structural or positional features compared to those without a clear angular preference. In the 30 mM sample, distinct pits exhibit markedly different preferential directions, even within the same sample. Furthermore, the fact that some pits within a single sample eject particles in nearly opposite directions suggests that the origin of the angular preference is more likely internal (e.g., local chemistry, hydrodynamics etc.) rather than driven by external factors (magnetic field etc). Appendix C display polar plots for other concentration that are also in accordance with these conclusions.

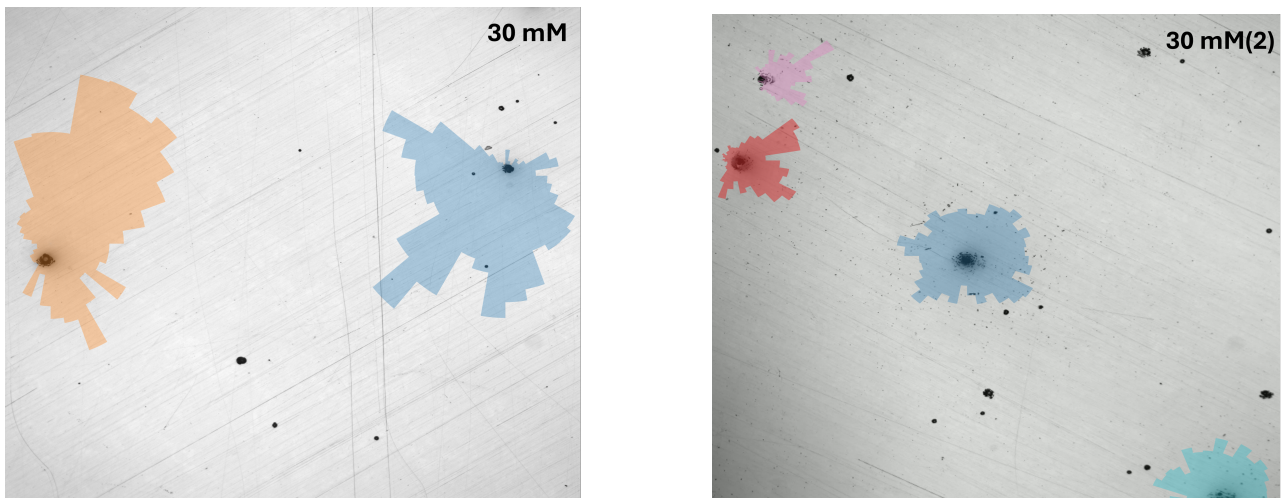


Figure 4: Polar plot of overall angles of ejections around considered pits

### 1.1.2 Correlation between pit's propagation and angle of ejection of particles

Another hypothesis is that the ejection direction of the particles may be influenced by the pit's internal structure—specifically, the direction in which the pit grows could play a determining role in the ejection angle.

To test this assumption, we analyzed the growth dynamics of the pits over time using frame-by-frame analysis. The procedure consisted of detecting the appearance of new pixels in the growing region of each pit from a frame to another. The angle of propagation was then computed using the same method described previously, with the exception that the reference point was set as the first pixel detected at the onset of pit formation. Figure 5 illustrates the newly appearing pixels between consecutive frames, highlighting the direction of pit propagation. The objective of this analysis is to investigate whether a correlation exists between the growth direction of the pits and the particle ejection angles discussed in the previous section.

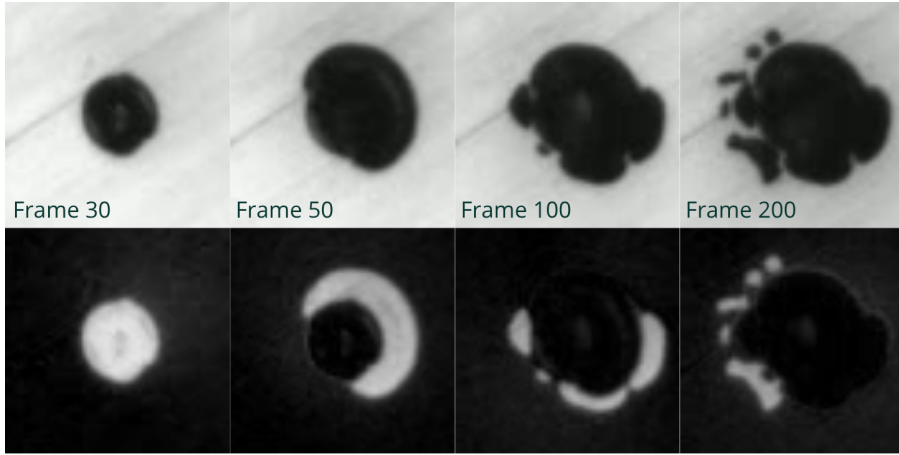


Figure 5: *Raw images of a single pit propagation at frame 30, 50, 100, 200 (top) and subtracted images at the same frame (frame 30 is subtracted with frame 0, frame 50 is subtracted with frame 30 ...) (bottom).*

Figure 6 presents the cross-correlation plot between the mean angle of each frame for particle ejection angles and the mean angle at each frame for pit propagation angles.

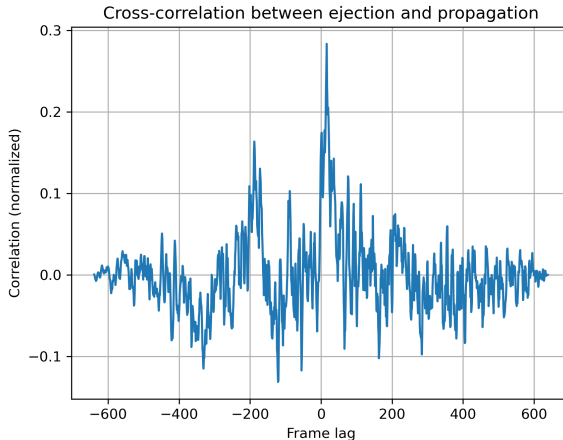


Figure 6: *Cross-correlation between the ejection angle of particles and propagation angle of pit versus the frame lag*

A maximum correlation of almost 0.3 is observed at a lag of approximately 10 frames, indicating that the ejection angle tends to align with the propagation angle roughly 10 frames later. The relatively low correlation value may be attributed to the limited accuracy in detecting all ejected particles, which introduces a bias in the calculation of the mean ejection angle at each frame.

### 1.1.3 Image treatment and general flux behavior

Mauzeroll et al. have proposed that the motion driving force of corrosion products during pitting originates from a density gradient induced by the newly formed metal oxides. This gradient gives rise to buoyancy forces, initially driving the surrounding solution downward toward the pit, and afterwards generating lateral flows that transport particles away from the pit<sup>9</sup>. Thus, the observed particles are not active agents but rather passive tracers of a hydrodynamic phenomenon associated with metal dissolution.

To test this hypothesis, we conducted a global analysis of the lateral motion of particles across the entire frame, with the aim of identifying potential hydrodynamic patterns that could support the proposed mechanism. The image processing methodology employed to detect and track particles throughout the frame is identical to the one previously described.

Figure 7 presents the global map of particle trajectories for both the 30 mM and 100 mM samples. Particle traces are shown in green, with each detected position marked frame by frame, and the final frame displayed for reference. Near the pit, the trajectories exhibit predominantly linear behavior, indicating directed motion. However, deviations from the initial paths are clearly observed when particles approach regions influenced by ejections from neighboring pits, suggesting local interactions or perturbations in the flow field. The hypothesis of electrostatic interactions between particles can be ruled out, as such behavior would have also been observed between particles originating from the same pit, which is not the case here. The observed deviations therefore support the presence of a hydrodynamic phenomenon governing particle motion. This phenomenon appears to generate distinct flow domains, which interact at their boundaries, resulting in a noticeable drift of the particles' initial trajectories upon contact. A possible explanation for the observed preferential ejection angles lies in the spatial arrangement and proximity of neighboring pits.

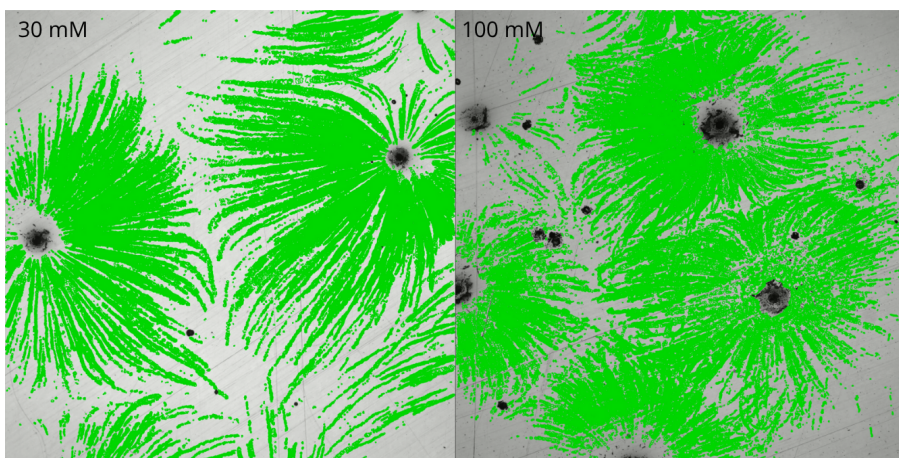


Figure 7: Corrosion products movement within the sample for 30 mM and 100 mM of NaCl in solution. Particle traces are shown in green.

This observation alone does not contradict the hypothesis proposed by Mauzeroll et al., as it remains compatible with the existence of a lateral flow. We then examined the vertical position of the particles during their ejection. Figure 8 illustrates the trajectory of a single particle from its point of ejection at the pit to its terminal position. Initially, the particle appears broad and blurred, and as it approaches its final position, it becomes progressively smaller and more intense. This behavior is characteristic of an out of focus object in optical microscopy, where variations in sharpness and intensity reflect changes in the vertical ( $z$ ) position relative to the focal plane. Given that only upward motion is possible along the vertical axis relatively to the substrate, we infer that frame 190 corresponds to the highest point reached by the particle, where it appears most blurred and least intense. Also, in frame 300, the particle is sharply defined and exhibits maximum intensity, indicating that it has reached the focal plane.

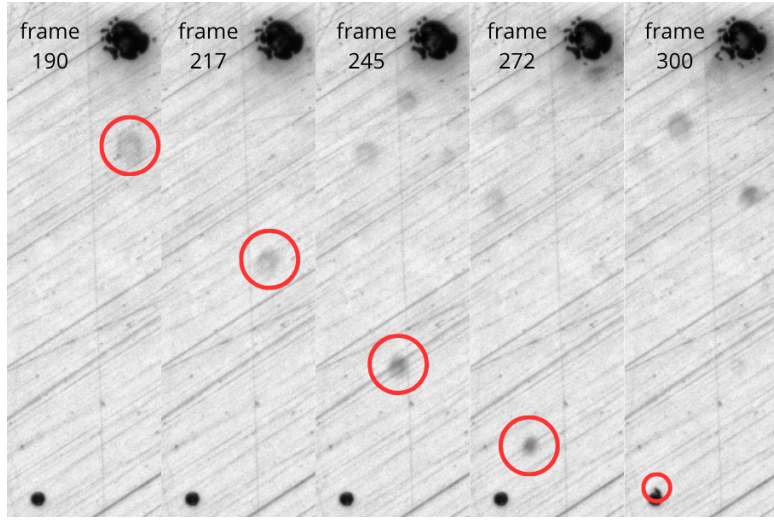


Figure 8: *Tracking of a single particle taken in the vicinity of a pit in a 30 mM sample. Red circle highlights the particle of interest.*

The observed trajectory is characteristic of a parabolic motion, suggesting a ballistic-like path. This upward movement of the particle supports the presence of an initial vertical component in its ejection. Consequently, this observation challenges the previously stated hypothesis of a purely downward fluid flux, as it clearly demonstrates an upward displacement inconsistent with such a flow.

#### 1.1.4 Particle trajectory outliers

Figure 8 also reveals that the tracked particle follows a parabolic ejection trajectory from a larger pit toward a smaller one, suggesting a potential form of communication or interaction between pits. Although this behavior is not systematically observed across all trajectories, it highlights the possibility of underlying mechanisms between pits.

Figure 9 shows the evolution of the velocity of this particle with frames. We can see a constant velocity after frame 20 until a small velocity peak around frame 103 which indicates an acceleration before the total stop of motion.

This velocity peak is also visually noticeable and occurs in the vicinity of the arrival pit, as illustrated in Figure 10, where the particle clearly accelerates as it approaches the pit.

This phenomenon could be attributed to the distinct chemical environments between the bulk solution, from which the particle is ejected, and the solution inside the pit. Indeed, the pit

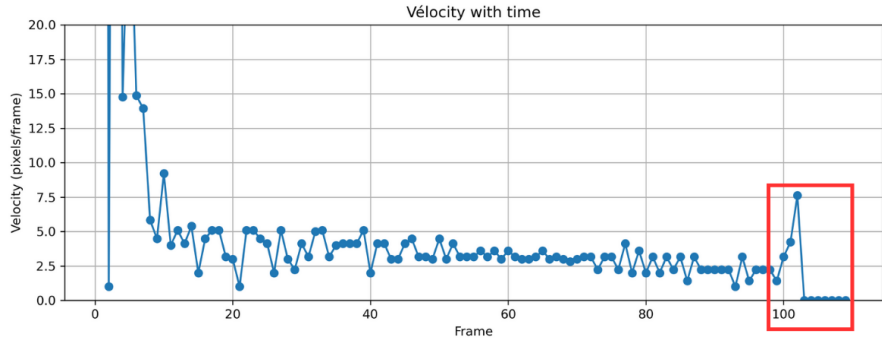


Figure 9: *Evolution of the velocity in px/frame of the considered particle in Figure 8 between frame 190 (being frame 0 on the x axis) and frame 300 (being frame 110 on the x axis). Red rectangle corresponds to a velocity outlier*

environment is known to exhibit a lower pH<sup>5</sup>, which may lead to the presence of metal ions at various oxidation states. As a result, the corrosion products within the pit could differ in oxidation state compared to those in the bulk solution<sup>10</sup>, potentially generating electrostatic interactions. These interactions may account for the observed acceleration of the particle as it approaches the pit.

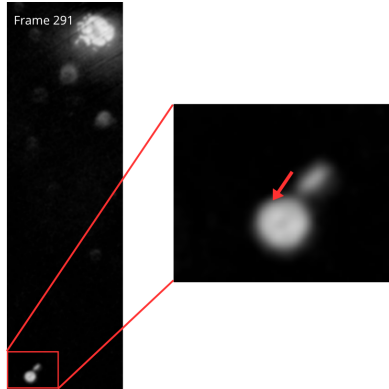


Figure 10: *Subtracted image of the considered particle and its surrounding at the frame 291. Corresponding to the moment right before the velocity peak. Red arrow points the direction of the particle movement.*

### 1.1.5 Limitations of classical computer vision tools

The vertical component of particle trajectories could provide a more complete understanding of their dynamic behavior. Since both the apparent size and intensity of a particle are directly influenced by its position relative to the focal plane, it becomes theoretically possible to estimate the z-position by experimentally calibrating the variation of intensity as a function of optical depth. However, such an approach requires highly reliable detection of particle shape and position. Traditional object tracking methods, such as contour detection using Canny edges<sup>11</sup> and contrast enhancement techniques like CLAHE<sup>12</sup>, previously employed in this study, have proven insufficient—particularly in the case of blurred or low-intensity particles, which are poorly segmented or entirely missed.

Figure 11 provides a representative example of the limitations encountered with classical detection methods, highlighting their inability to accurately segment low-intensity or blurred

particles.

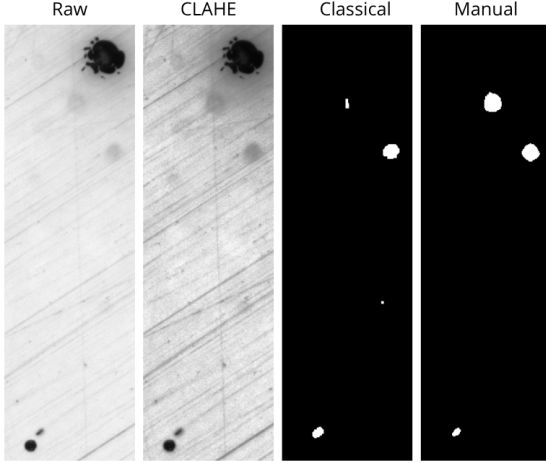


Figure 11: *Raw image (Raw), enhanced contrast image with CLAHE (CLAHE), particle segmentation using state of the art contouring / morphological treatment (Classical) and manual segmentation of particles (Manual)*

In fact, contrast enhancement techniques such as histogram equalization used in CLAHE to improve the visibility of low-contrast objects like our blurred particles, present a significant drawback: they tend to darken the regions surrounding the pits. As a result, particle detection becomes considerably more difficult near the pit, leading to a loss of information about their trajectories during the initial phase of ejection. As shown in Figure 11, the particle located closest to the pit appears cropped and cannot be properly segmented when compared to manual segmentation.

## 1.2 Deep learning approach : enhanced particle segmentation and detection using CNNs

To overcome these limitations, a deep learning-based approach was adopted. The problem at hand corresponds to a semantic segmentation task, where the objective is to identify the pixels that belong to corrosion particles. By first constructing a reliable labeled dataset through manual annotation, and then training a convolutional neural network capable of learning relevant particle features, we aim to achieve accurate and consistent segmentation of the particles across all frames.

The objective of this section is to implement a convolutional neural network (CNN) architecture known as U-Net<sup>2</sup>, a state-of-the-art model widely used in medical and biomedical image segmentation. Our aim is to adapt this architecture to our specific application and fine-tune it in order to achieve optimal segmentation performance.

### 1.2.1 U-Net architecture and training

The U-Net architecture is composed of two main parts: an encoder (downward path) and a decoder (upward path). The encoder consists of successive convolutional layers (blue arrows), which extract relevant features from the input images in the form of feature maps, and max-pooling layers (red arrows), which progressively reduce the spatial resolution while preserving essential information (downsampling). The decoder, in turn, reconstructs the segmentation

mask by gradually upsampling the feature maps and integrating the information learned during the encoding phase. At each convolutional stage, the number of feature maps increases, each representing a specific characteristic extracted from the original image, while the spatial resolution decreases accordingly. The number of feature maps at each stage of the network is defined by the user and constitutes a hyperparameter that can significantly influence the quality of the segmentation. Figure 12 illustrates the architecture of a U-Net model with 64, 128, 256, and 512 feature maps, respectively, at successive convolutional stages. A key characteristic of U-Net is the presence of skip connections (indicated by grey arrows), which allow the transfer of spatial information from the encoder to the decoder path. These connections help recover fine structural details that may have been lost during the downsampling process.

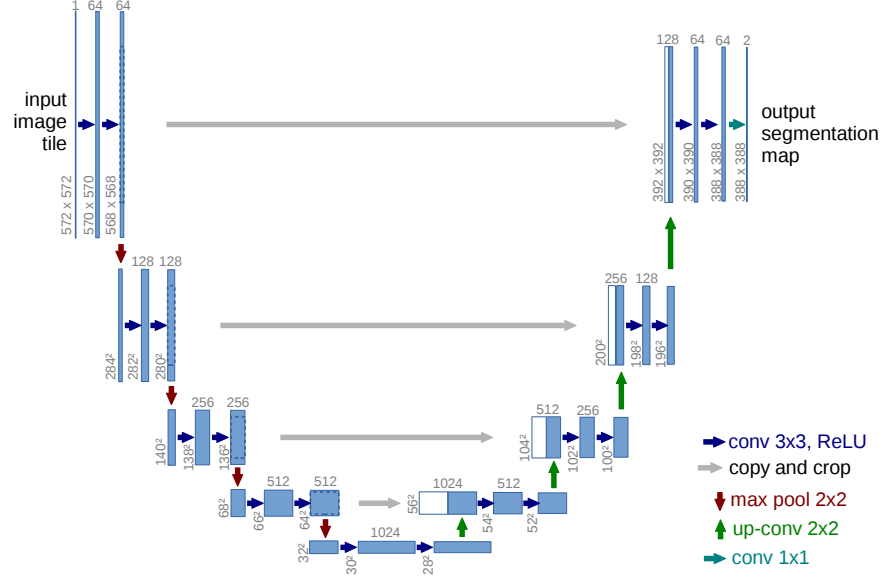


Figure 12: *U-Net architecture*<sup>2</sup>

The U-Net model was implemented using the Python libraries PyTorch and TensorFlow. It requires, as input, raw images of the sample along with corresponding annotated masks, in which pixels belonging to corrosion particles are explicitly labeled while all other regions are marked as background. These annotated masks serve as ground truth during training, enabling the model to iteratively adjust its parameters and improve its segmentation performance through supervised learning.

The main challenge lies in accurately annotating the particles within the images. A commonly used strategy consists in labeling each pixel individually, which is not realistically feasible due to the time and effort required. An alternative approach involves leveraging advanced annotation tools, such as the Segment Anything Model (SAM)<sup>13</sup>, developed by Meta, which significantly accelerates the annotation process while maintaining high precision. Features maps size and all parameters relative to the training of U-Net are presented in Appendix D. Another challenge arises from the ratio between the particle size and the overall image dimensions. Indeed, the original images have a resolution of  $2240 \times 2252$  pixels, while even the largest particles occupy only a few dozen pixels. This scale discrepancy makes it difficult for convolutional neural networks to effectively detect such small features. To address this issue, each image was divided into multiple tiles of  $200 \times 200$  pixels. This tiling approach increases the relative size of the particles within each tile, thereby facilitating their detection and improving the performance of the segmentation model.

Figure 13 presents an example of a single tile, alongside its corresponding ground truth mask and the predicted segmentation obtained after training the model on a limited dataset of 100 images.

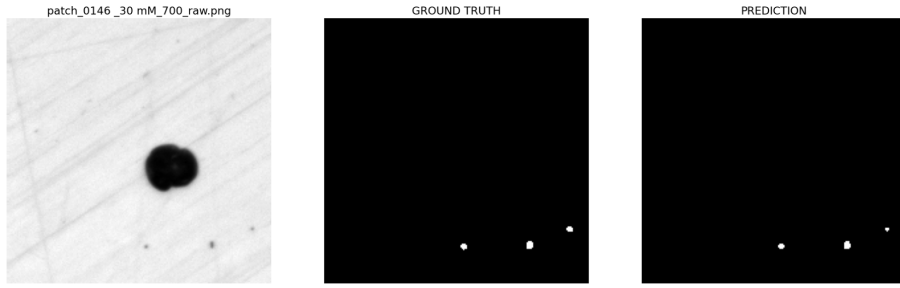


Figure 13: *Slice of a raw image, manually labeled image (GROUND TRUTH) and prediction of the model (PREDICTION) for a 30 mM sample.*

The U-Net model was trained on a limited dataset comprising 100 images, with 70 images used for training and 30 reserved for validation. Model's performance have been measured while changing hyperparameter such as the number of epochs and the learning rate in order to found the best fitted hyperparameters for the detection of particles.

### 1.2.2 Model performance

To evaluate the model's performance, five metrics were selected: F1-score, accuracy, recall, and precision. These metrics are computed based on the classification of individual pixels into four categories: true positives (TP), corresponding to the number of pixels that belong to the object and are correctly predicted as such; true negatives (TN), corresponding to the number of background pixels correctly identified as not belonging to the object; false positives (FP), referring to background pixels incorrectly classified as object pixels; and false negatives (FN), which are object pixels that the model failed to detect.

The accuracy score reflects the proportion of correct predictions over the total number of predictions. Precision measures the proportion of true positives among all pixels predicted as belonging to the object. Recall, on the other hand, quantifies the proportion of true positives relative to all actual object pixels. The F1-score corresponds to the harmonic mean of precision and recall, providing a balanced metric that accounts for both false positives and false negatives. Each metrics formula is available in Appendix A.

Table 1 presents performance metrics for different values of number of epochs, corresponding to the number of times the model has seen each image, and various learning rates, which define the step size at which the model updates its parameters during training.

The best performance was obtained with a higher number of epochs and a lower learning rate. Specifically, the combination of 100 epochs and a learning rate of 0.001 yielded the most favorable metrics. Additionally, we observed consistently high accuracy values, regardless of the training configuration. This can be attributed to the very small size of the particles relative to the overall image: the majority of pixels belong to the background, which the model predicts correctly, thus artificially increasing the accuracy. As a result, accuracy is not a reliable metric in this context and should not be used to determine segmentation performance.

Given the small size and often blurred appearance of the particles—sometimes barely distinguishable from the background, the use of a high number of epochs and a low learning rate is

justified. These settings allow the model to gradually learn fine-grained features and contextual clues necessary for accurate particle segmentation.

	EPOCHS					LEARNING RATE				
	15	30	50	70	100	0.0005	0.001	0.005	0.01	0.1
<b>F1 SCORE</b>	0,37	0,18	0,7	0,73	0,75	0,7	0,74	0,54	0,39	0,58
<b>ACCURACY</b>	0,2	0,99	0,99	1,0	1,0	1,0	1,0	1,0	0,99	0,99
<b>RECALL</b>	0,1	0,1	0,6	0,61	0,7	0,63	0,70	0,40	0,26	0,64
<b>PRECISION</b>	0,8	0,77	0,78	0,82	0,80	0,79	0,79	0,84	0,79	0,54

Table 1: *Performance table of U-Net at different values of epochs and learning rate. Performance at different learning rates have been calculated at 100 epochs*

Figure 14 presents a comparison between segmentation masks obtained via classical image pre-processing and contour detection techniques, and those predicted by the U-Net model. While the pre-processed masks detect a larger number of particles, they exhibit poor segmentation accuracy, particularly in the vicinity of the pit. In contrast, the U-Net model demonstrates a significantly higher precision in delineating particle boundaries, even for particles located near the pit, thus enabling their tracking from the very onset of ejection.

It is worth noting that the U-Net was trained on a limited dataset of only 100 images. As such, its performance could be substantially improved by increasing the size and diversity of the training set.

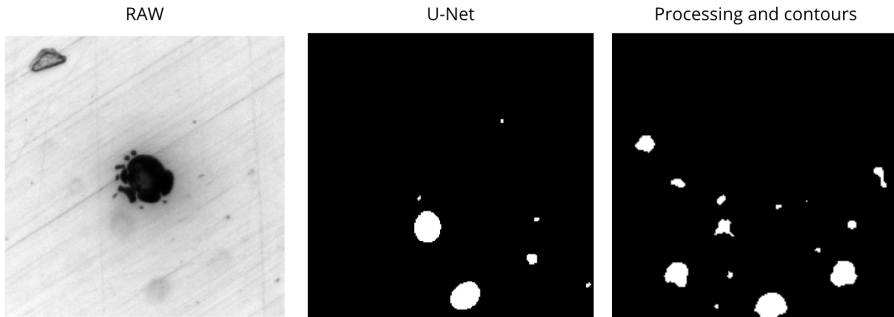


Figure 14: *From left to right : raw image, predicted mask of particles by U-Net and obtained mask using state of the art image processing and contouring.*

## Conclusion

At first, through image processing and object detection using python algorithms, we were able to provide precious data relative to the dynamics of corrosion products during pitting corrosion. Their angle of ejection could be explained by an unknown hydrodynamic phenomenon influencing neighboring pits and effecting their direction of ejection. Also, pit propagation direction seems to play a role in the direction of ejection of particles. We also highlighted the presence of a vertical component to the ejection trajectory which was not observed in the literature. Trajectory analysis has also raised the presence of outliers such as a gain of velocity of a particle in the vicinity of a pit, bringing out the possibility of electrostatic forces between corrosion products in the bulk solution and products in the pit.

Even though such image treatment procedures succeeded on giving important information, it shows limitations such as poor segmentation ability around pits, resulting in a loss of information on their trajectory at the very beginning of their ejection. This main limitation justifies the necessity of using advanced procedures in order to accurately detect and track ejected particles. Deep learning is one of the best way to respond to this kind of semantic segmentation problematic. We have seen that state of the art convolutional neural network U-Net shows great performance on segmenting our particles.

Overall, most of the results found during this study needs to be clarified experimentally by analysis such as XPS for the composition of the our passive layer, Raman spectroscopy for the composition of corrosion products, in-situ probing of the pH in the pit during pitting corrosion. But we demonstrated, through this study, that data and image analysis using computer vision and Deep learning tools could be a good support to provide new perspectives to an area of chemistry that has been largely undeveloped in recent years.

## Bibliography

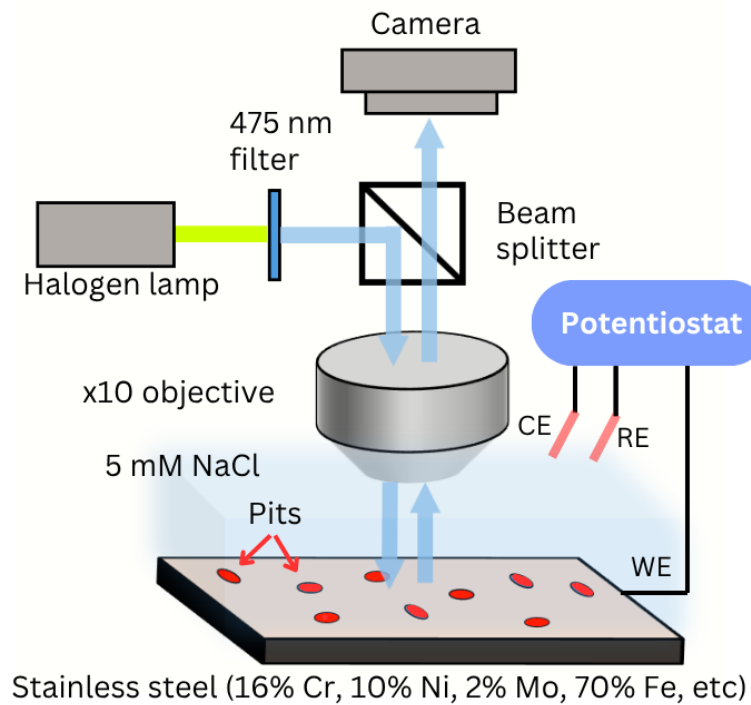
- [1] A. Makogon, F. Kanoufi and V. Shkirskiy, *Chemical Communications in Pitting Formation: A Multi-Faceted Study on Pitting Corrosion in Steel using Optical Microscopy, Machine Learning, and Physical Modeling*, Poster presented at scientific meeting, 2023, aleksei.makogon@cnrs.fr.
- [2] O. Ronneberger, P. Fischer and T. Brox, *U-Net: Convolutional Networks for Biomedical Image Segmentation*, 2015, <https://arxiv.org/abs/1505.04597>.
- [3] A. Makogon, L. Bertolucci Coelho, J. Ustarroz, P. Decorse, F. Kanoufi and S. SHKIRSKIY, *ChemRxiv*, 2025.
- [4] P. Pistorius and G. Burstein, *Philosophical Transactions of The Royal Society A: Mathematical, Physical and Engineering Sciences*, 1992, **341**, 531–559.
- [5] G. S. Frankel, *Journal of The Electrochemical Society*, 1998, **145**, 2970a.
- [6] P. Li and M. Du, *Corrosion Communications*, 2022, **7**, 23–34.
- [7] A. Makogon and S. SHKIRSKIY, *Original data and codes for "Machine Learning- Enhanced Optical Monitoring for Identifying Pitting-Susceptible Zones in 316L Stainless Steel" article*, 2025, <https://doi.org/10.5281/zenodo.14653184>.
- [8] M. Islam, S. A. Karim and M. Faris, 2024.
- [9] L. Grandy, R. Lacasse, J. R. Adsetts, C. Hitz, D. Chhin and J. Mauzeroll, *Corrosion Science*, 2024, **241**, 112518.
- [10] B. Morgan and O. Lahav, *Chemosphere*, 2007, **68**, 2080–2084.
- [11] H. Agrawal and K. Desai, *International Journal of Technical Research Science*, 2024, **9**, 27–35.
- [12] P. Musa, F. Rafi and M. Lamsani, 2018, 1–6.
- [13] A. Kirillov, E. Mintun, N. Ravi, H. Mao, C. Rolland, L. Gustafson, T. Xiao, S. Whitehead, A. C. Berg, W.-Y. Lo, P. Dollár and R. Girshick, *Segment Anything*, 2023, <https://arxiv.org/abs/2304.02643>.

## Appendix

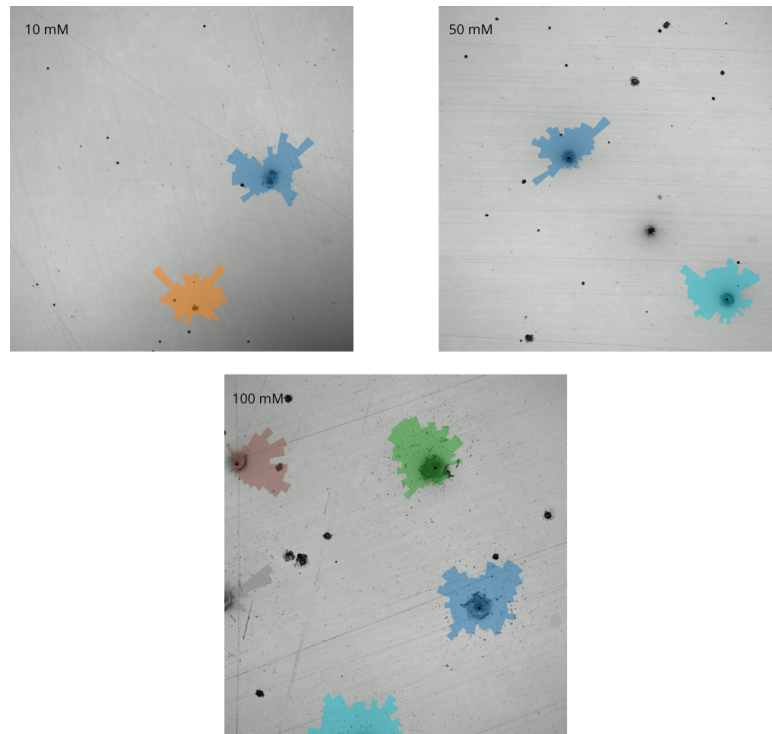
### A- U-Net metrics formulas

- $F1\ Score = \frac{precision * recall}{precision + recall}$
- $Precision = \frac{TP}{TP+FP}$
- $Recall = \frac{TP}{TP+FN}$
- $Accuracy = \frac{TP+TN}{TP+FN+FP+FN}$

### B- Recording set up of pitting corrosion using potentiostate and microscope



### C- Polar plot with overall ejection angles for 10 mM, 50 mM and 100 mM samples



### D- Parameters for U-Net training

```
{'encoder': 'timm-efficientnet-b0',
 'weights': 'imagenet',
 'resize': 224,
 'nb classes': 1,
 'epochs': 100,
 'lr': 0.001,
 'gamma': 0.85,
 'batch size': 5}
```

features maps = [64,128,256,512]

### E- Code and images used

[https://github.com/AnesSAD/Pitting\\_corrosion-CNRS.git](https://github.com/AnesSAD/Pitting_corrosion-CNRS.git)